PRECIPITATION EFFICIENCY CONSTRAINT ON CLIMATE CHANGE

Ryan L. Li[1*], Joshua H.P. Studholme[1], Alexey V. Fedorov[1], Trude Storelvmo[2]

1. Department of Earth and Planetary Sciences, Yale University
   210 Whitney Avenue, New Haven CT 06511
2. Department of Geosciences, University of Oslo
   Gaustadalléen 21, Bygning H, plan 3, Forskningsparken
   0349 Oslo, Norway

* Corresponding author

In principle accepted for Nature Climate Change as an Article

Corresponding author address: Ryan L. Li, 210 Whitney Avenue, New Haven, CT 06511, Tel: (203) 432-3114, E-mail: ryan.li@yale.edu.

ABSTRACT

Precipitation efficiency (PE) relates cloud condensation to precipitation and intrinsically binds atmospheric circulation to the hydrological cycle. Due to PE's inherent microphysical dependencies, definitions and estimates vary immensely. Consequently, PE's sensitivity to greenhouse warming and implications for climate change are poorly understood. Here, we quantify PE's role in climate change by defining a simple index ϵ as the ratio of surface precipitation to condensed water path. This macroscopic metric is reconcilable with microphysical PE measures and higher ϵ is associated with stronger mean Walker circulation. We further find that state-of-the-art climate models disagree on the sign and magnitude of future ϵ changes. This sign disagreement originates from models' convective parameterizations. Critically, models with increasing ϵ under greenhouse warming, in line with cloud-resolving simulations, show greater slowdown of the large-scale Hadley and Walker circulations and a two-fold greater increase in extreme rainfall than models with decreasing ϵ.

Precipitation efficiency (PE) quantifies the fraction of condensed water in a cloud to reach the surface as precipitation. In the tropics, precipitation is dominated by highly transient, spatially restricted, deep convective events driving intense upwards mass fluxes that, in aggregate, compose the ascending branches of the meridional Hadley and zonal Walker circulations. As an air parcel rises within a cumulus cloud and some of the water vapor it contains condenses, it rains out a fraction of its water content leaving the remaining condensate to interact with incoming and outgoing radiation. Some of the precipitation evaporates as it falls back through the atmosphere, which cools the air and directly drives local downward mass fluxes. A higher PE implies lower evaporation of hydrometeors and greater net latent heat release by convective towers. Total cloud condensation and re-evaporation of falling precipitation are both macrophysical manifestations of inherently microphysical processes. PE can be applied to larger scales by considering a *cloud ensemble* - the statistical average over multiple transient deep-convective updrafts and downdrafts [1].

Environmental controls on PE can be combined into three groups: cloud microphysics, entrainment and convection dynamics [2], but work to understand how these controls relate to climate and anthropogenic influence is only now coming to the fore. A recent local-scale observational study at Darwin, Australia found that PE increases with free-tropospheric humidity and decreases with both surface temperature (T_s) and convective available potential energy [3]. In contrast, limited domain cloud-resolving model (CRM) studies of radiative convective equilibrium indicate that PE increases with T_s [4, 5]. Further, aerosol loading can also modulate PE in shallow and deep clouds by modifying microphysical processes [6, 7].

Changes in PE are of significant interest because they could relate to a number of changes at planetary and smaller scales in contemporary climate. Firstly, since PE controls the relationship between upward and downward convective mass fluxes and aggregate convective mass fluxes result in large-scale overturning, PE may provide insight into how the tropical circulation responds to greenhouse gases [1]. Secondly, limited-domain cloud resolving modeling indicates that the microphysical processes encapsulated by PE [4, 8] may be useful in understanding projections of increases in precipitation extremes with warming [9]. Lastly, since higher PE results in less detrainment of cloud condensate at high altitudes, PE has been hypothesized to play a role in cloud feedback [10-14].

In a warmer atmosphere, it is unclear whether PE will decrease [3], remain constant [15, 16], or increase [4, 5, 17]. A theoretical constraint on PE based on an entraining plume model is that PE should be greater than or equal to one minus relative humidity [18]. This is, however, only a weak constraint for PE as updrafts are typically near saturation. With higher temperature and more radiative cooling, precipitation increases and convective mass flux decreases [1]. This implies an increase in the intensity of precipitation or increase in PE, but this expectation is unconfirmed in observations and models alike. Global Climate Models (GCMs) predict a robust increase of 2-3% in global precipitation per degree Celsius (°C) of warming [19, 20]. Meanwhile, cloud condensation is sensitive to a multitude of environmental conditions such as tropospheric temperature, humidity, and stratification, and may increase [5] or decrease [21] with warming at different altitudes. Thus, changes to PE – being the ratio of precipitation to condensation – are equivocal.

The question of how PE will change with warming is challenging to address, due to the wide diversity in PE definitions across studies using observations, CRMs, and GCMs (see [22] for the latest review). Definitions of PE can be generally categorized into large-scale PE ϵ_{ls} and cloud microphysical PE ϵ_m [23]. ϵ_{ls}, the ratio of surface precipitation P_s to the sub-cloud water vapor convergence, has been widely used to study thunderstorms. ϵ_{ls} takes values ranging from 0.1 to greater than 1 [24] depending on environmental factors, such as vertical wind shear, sub-cloud humidity, and cloud base areal extent [25]. However, this measure of PE is limited to studying individual convective events. When averaged over space and time, ϵ_{ls} is by definition equal to unity since what goes up must come down. As ϵ_{ls} is sensitive to the spatial and temporal scales considered [26], it is inappropriate for climatological PE analysis.

By contrast, ϵ_m – the ratio of P_s to the column-integrated condensation rate C – is typically less than unity over various spatiotemporal scales owing to the evaporation of falling hydrometeors before they reach the surface as precipitation. However, ϵ_m is difficult to directly observe due to its inherent microphysical dependence. The typical range of ϵ_m averaged over a limited domain CRM in radiative convective equilibrium is 0.2 to 0.5 [5, 27, 28], which is similar to that inferred in observational studies of tropical convection [29], mid-latitude squall lines [30], and mid-latitude cyclones [31]. The magnitude of ϵ_m is sensitive (up to 50% relative change) to the computational implementation of condensate removal in the CRM [5], which occurs at multiple levels simultaneously.

Given the inherent problems in using ϵ_{ls} and ϵ_m across different models and observations, the goal of this paper is to introduce a simple physical measure of PE applicable across different spatial scales to serve as a metric linking the macro and microphysical approaches. We will then quantify the relation between PE and the mean climatological state in the tropics and investigate the role of PE in climate change.

DEFINING A PRECIPITATION EFFICIENCY MEASURE

In this study, we define a PE measure as:

$$\epsilon = \frac{P_s}{CWP}\ [units: s^{-1}] \quad (1)$$

where CWP is the condensed water path, i.e., the column integrated cloud liquid and ice content. See *Methods* for a brief discussion of the uncertainties. Similar expressions have been used in previous studies for water vapor cycling [31] and warm clouds [17, 32]; ϵ differs from those in that it uses the total condensate budget. Since PE is a manifestation of microphysical processes, it is critically important that an index quantifying it can be linked to this microphysics. Limited domain CRM studies have been able to explicitly compute microphysical ϵ_m by outputting condensation rates at each vertical level [5]. However, this is not feasible in climatological observations of nature nor in GCMs. Therefore, we validate the use of ϵ as a measure of PE by running a set of CRM experiments (Methods) and computing both ϵ and ϵ_m. The macrophysical ϵ of Equation (1) is tightly correlated to the microphysical ϵ_m ($r = 0.86$; Extended Fig. 1 and Extended Fig. 2). The exclusive use of macrophysical variables in ϵ enables comparison between observations, CRMs, and GCMs.

Unlike the parameter ϵ_m, the present formulation for ϵ is dimensional. As such, it is a general measure or index of PE and not an efficiency defined as a fraction of unity. For brevity and given the tight correlation of ϵ with ϵ_m, we herein refer to the parameter ϵ as PE.

The ϵ metric could be calculated at various spatial and temporal resolutions. Within time-space aggregated values, the average is composed of a variety of cloud types, such as non-precipitating shallow clouds and mixed-phase clouds. Within each of these cloud types, PE will vary in correspondence with the relevant cloud physics. We use climatological ϵ to represent the net effect of these clouds within the tropical cloud ensemble.

The inverse $\epsilon^{-1} = \tau$ is a characteristic residence timescale for the total condensed cloud water across an ensemble of cloud types, or a characteristic drying timescale for the atmosphere if condensation has stopped. Satellite-based observations indicate a tropical-mean τ of about 46 minutes (Fig. 1; [33]). This low τ value reflects the vigorous hydrological cycling of the atmosphere, constantly requiring high rates of condensation to maintain the atmospheric stock of CWP. In this timescale interpretation, precipitation is assumed to be a first-order process within the CWP budget (*Methods*). This assumption holds well in satellite observations (Fig. S1) and, to some degree, in GCMs. As such, we think of ϵ as an emergent diagnostic linked to the drying timescale of the atmosphere. Its value is close to, but slightly different from the e-folding rate of condensed water removal.

The spatial pattern of annual-mean observed ϵ is broadly correlated with regions of high climatological precipitation (Fig. 1a). Regions of high ϵ ($> 0.8 \times 10^{-3} s^{-1}$) are tropical convergence zones with intense time-mean precipitation, such as the Indo-Pacific warm pool (WP; 20S-20N, 80E–170E). Low ϵ ($< 0.2 \times 10^{-3} s^{-1}$) is found in subsidence regions such as the Eastern Pacific (EP; 20S–20N, 140W–80W) and Atlantic subtropics. Local ϵ can be large due to small CWP, such as on the coast of the Arabian Peninsula, but these arid regions have little climatological precipitation and ϵ is thus not a suitable index there. Over the WP, ϵ increases spatially with T_s. Deep convection preferentially occurs over warm SSTs and this favors stronger updrafts and more precipitation. From 26 to 29°C, ϵ doubles from $0.4 \times 10^{-3} s^{-1}$ to $0.8 \times 10^{-3} s^{-1}$, halving the residence time (Fig. 1b). With reduced residence time, microphysical processes such as re-evaporation of raindrops and entrainment of dry and less buoyant air are less effective at reducing the flux of hydrometeors reaching the surface. This corresponds to weaker downdrafts and greater net latent heat release by convective updrafts.

The observed interannual standard deviation of tropical ϵ is 2.8%. The 2002-2020 period of these available observations includes the global warming hiatus [34], hindering the monitoring of the temperature sensitivity of ϵ. Regional magnitudes of ϵ are sensitive to T_s, which is dominated by the inter-annual variability of sea surface temperatures (SSTs) in the Pacific Ocean (Fig. 2). During El Nino, when the EP warms due to suppressed ocean upwelling, the zonal SST gradient is reduced. The atmosphere responds with more frequent deep convection, resulting in more cloudiness and higher P_s in the central and eastern Pacific. This is corroborated by a positive correlation ($r = 0.60$) between the Nino3.4 SST index and EP-mean ϵ, and a negative correlation between the Nino3.4 index and ϵ averaged over the WP, ϵ_{WP} ($r = -0.74$; Extended Fig. 3). During El Nino, ϵ_{WP} is lower and ϵ averaged over the EP is higher (Fig. 2). The regionally different responses of ϵ to underlying SST, combined with the ENSO correlations, reveal the significance of non-local dynamics on local PE.

LINKING PE TO THE TROPICAL MEAN-STATE

We find significant negative temporal correlations between the observed monthly Outgoing Longwave Radiation (OLR) and ϵ_{WP} (Fig. 3a). The local OLR vs. ϵ_{WP} correlations are particularly strong over the WP and equatorial South America, associating high PE with deep convection of higher intensity or frequency. The sign of the observed convection-PE relationship in the WP is captured by the ERA5 reanalysis and the majority of CMIP6 models (Fig. S2). Consistent with these correlations, over the past two decades, there was an intensification of WP precipitation [35] coinciding with trends of increased occurrence frequency of deep anvil clouds [36].

The correlations between OLR and ϵ_{WP} in Fig. 3a display a similar spatial pattern to the mean-state Walker circulation. This is seen in negative correlations in the dominant ascending branches over the WP and northern South America and positive correlations in descending branches over the subtropical eastern Pacific and equatorial Atlantic. The strength of the Pacific Walker circulation, measured by the mean sea level pressure difference ($dSLP$) between the western and eastern equatorial Pacific (*Methods*), is robustly correlated with ϵ_{WP} across CMIP6 models ($r = 0.63$; Fig. 3b). High PE implies a greater rate of net latent heat release by precipitation per convective cloud. Concurrently, a stronger Walker circulation is sustained, with stronger ascending motion in the WP. Although observationally-based ERA5 data also exhibits a positive correlation between ϵ and Walker Circulation strength of similar magnitude (not shown), this relationship is complicated by strong El Niño impacts on ϵ.

CHANGES IN ϵ WITH GREENHOUSE WARMING

During periods covered by satellite observations (2002-2020) and reanalysis (1979-2021) tropical mean temperature variability is constrained to within 0.5 °C. These records are unfortunately therefore limited guides to the sensitivity of ϵ to T_s, $\partial\epsilon/\partial T_s$. By contrast, the CMIP6 ensemble explores tropical temperature increases up to 4 °C in a large number of individual models (Fig. 4). We find very large dispersion between CMIP6 models in the slope of $\partial\epsilon/\partial T_s$. After 2 °C of warming, the ensemble mean PE response is 2.5%, with an intra-model range of -7% to $+12\%$. This range reflects relative changes in both P_s and CWP (Extended Fig. 4). Intra-model diversity in the representation of convection is a likely cause of this wide range in ϵ sensitivity. Given this, we use a limited domain cloud resolving model SAM (Methods) in which convection is explicitly resolved to explore the range of tropical temperatures found in the CMIP6 SSP5-8.5 simulations of twenty-first century anthropogenic warming. In these SAM simulations, ϵ increases with temperature (Fig. 4), consistent with a previous study [5] that used the same model but studied a microphysical measure of PE.

While the relationship between convective aggregation and warming remains an unsettled research question [37], convective aggregation prefers warmer SSTs and is associated with high PE [38]. Within aggregated convection, precipitation falls through columns of high humidity air, resulting in less evaporation and implying higher PE [39]. On the other hand, the abundance of clear-sky regions in aggregated convection favors the presence of boundary layer clouds which typically re-evaporate with near zero PE [5]. We investigate these competing effects upon cloud ensemble PE by running two sets of SAM simulations – a large domain (1024 by 1024 km^2, SAM-L) and a small domain (512 by 512 km^2, SAM-S). Self-aggregation of convection is known to be inhibited in smaller domain sizes [37] and indeed the principal difference between SAM-L and SAM-S is that convection is aggregated in the former and disaggregated in the latter (Extended Fig. 5). In the absence of self-aggregation, ϵ increases with T_s at a rate of 2% per °C. When convection is aggregated, $\partial\epsilon/\partial T_s$ increases to a rate of 5% per °C. This suggests that the impact of reduced evaporation of rainfall (raising cloud ensemble PE) dominates over the impact of more prevalent low clouds (lowering cloud ensemble PE). While the sign of these CRM-estimated $\partial\epsilon/\partial T_s$ are positive, consistent with [5], its magnitude may depend on precipitation microphysics in the CRM, requiring future work.

Generally, there exists two groups of GCMs in Fig. 4, divided cleanly on the sign of their sensitivity of ϵ to T_s: (1) models in which ϵ increases with T_s and (2) models in which ϵ decreases with T_s. We find that this disagreement can be traced to whether or not precipitation is represented as dependent (e.g. [40]) or independent (e.g. [41]) of ascending mass flux in a convective grid cell within these GCM's convective parameterizations (see Supplementary Table 1). The mass-flux dependence of convective precipitation allows higher ϵ when the environmental conditions favor strong vertical ascent. This dependence is absent in GCMs with convective precipitation proportional to cloud water only, which collectively show weak or negative sensitivity of ϵ to T_s. The response of ϵ to warming in models that possess this mass-flux dependence is similar in magnitude and slope to those predicted by CRM simulations. The magnitude of mean-state ϵ in some models can be different up to a factor of 2-3 compared to observations and CRMs, which should be noted and requires future work (Fig. S3). Thus, a longer record of ϵ is required to confirm the positive $\partial\epsilon/\partial T_s$ relationship predicted by the CRM and the CMIP6 GCMs with updraft dependent precipitation parameterizations.

IMPLICATIONS FOR FUTURE CLIMATE

Next, we investigate the role of precipitation efficiency in climate change, focusing on several key interwoven questions: *What role does PE play in controlling the response of large-scale atmospheric circulation, temperature distribution and precipitation extremes to greenhouse warming? Does the sign of $\partial\epsilon/\partial T_s$ across CMIP6 models affect climate change projections?*

The tropical circulation is expected to weaken under anthropogenic climate change from both dynamic [42] and thermodynamic [43] perspectives. GCMs generally predict the Hadley cells will widen and weaken in the twenty-first century [44]. The Southern Hemisphere cell's response is expected to be dominated by widening, while the Northern Hemisphere cell is predicted mostly to weaken [45], consistent with the changes shown in Fig. 5. The predicted magnitudes of Northern Hemisphere Hadley cell weakening are highly variable between models in CMIP5 [44] and CMIP6 (this lack of consensus is visualized as the absence of shading between 5–30ºN in Extended Fig. 6). This range in predictions is not well understood [45]. We find here that much of this intra-model disagreement in projected Northern Hemisphere Hadley cell slowdown (Extended Fig. 6) is directly aligned with differences in the warming response of PE (Fig. 5b).

Binning GCMs into two groups based on the sign of $\partial\epsilon/\partial T_s$, we find that models with positive $\partial\epsilon/\partial T_s$ exhibit stronger warming responses (Fig. 5a) and amplified reductions of the zonal-mean mass streamfunction ψ under greenhouse warming (Fig. 5b). Robust weakening signals are present in the Hadley Circulation northern and southern branches, indicated by the opposite sign of present-day ψ and its warming response $\Delta\psi$. Regional differences in $\Delta\psi$ can be as large as 30%. These results suggest that, all else being equal, models with positive $\partial\epsilon/\partial T_s$ possess efficient deep convective towers that collectively release more net latent heat (or equivalently, have less evaporative cooling). On the other hand, deep convective towers become less efficient in models with negative $\partial\epsilon/\partial T_s$, requiring a stronger circulation to sustain more latent heating. This argument conforms to the mass flux view [43] of tropical circulation slowdown Fig. S4). Considering the difference in the maximum overturning as a measure of Hadley cell intensity, positive $\partial\epsilon/\partial T_s$ corresponds to 4.5% more weakening of the northern cell compared to negative $\partial\epsilon/\partial T_s$ (Fig. 6). This difference in Hadley circulation weakening north of the equator, reduced when normalized by temperature (Extended Fig. 7), is strongly coupled to the overall planetary temperature response. Weakening of the southern cell is less pronounced in CMIP6 [45] and hence the differences between model groups are not statistically significant.

The Pacific Walker circulation also exhibits relative changes different between the two model groups. Measured by the subsiding pressure velocity in the eastern equatorial Pacific (*Methods*), the Walker circulation weakens by 30% in positive $\partial\epsilon/\partial T_s$ models compared to 16% in negative $\partial\epsilon/\partial T_s$ models, (Fig. 6). Thus, the demonstrated link between future changes in ϵ and the large-scale circulation suggests that the assumption of constant PE in changing tropical circulations is inadequate. After normalizing by temperature (Extended Fig. 7), these differences are less pronounced but remain statistically significant, suggesting both dynamic and thermodynamic contributions to the Pacific Walker cell response.

We also find that the expected increase in extreme precipitation under climate change [46], measured as the 99.9th percentile of daily-mean precipitation ($P_{99.9}$), is more than twice as strong in positive $\partial\epsilon/\partial T_s$ models than in negative $\partial\epsilon/\partial T_s$ models. Specifically, global $P_{99.9}$ increases 19.5% in positive $\partial\epsilon/\partial T_s$ models, versus only 9.4% in negative $\partial\epsilon/\partial T_s$ models. These differences remain statistically significant after normalizing $P_{99.9}$ by effective climate sensitivity (Extended Fig. 7). This implies that the CMIP6 ensemble estimate of precipitation extreme increase could underestimate the true value by over a third, in line with the results of [47]. This result quantifies the microphysical contribution to hydrological cycle sensitivity, generally divided only into dynamic and thermodynamic contributions.

Aerosol and indirect greenhouse gas effects can add higher order complexity to the temperature related effects on ϵ discussed in the present study. This can be further explored in existing model intercomparison projects such as Ref [48], an avenue for future work.

In summary, we have defined and explored the observed climatology of the PE index, ϵ, its temporal variation and link to the large-scale tropical circulation and precipitation extremes. We find that the CMIP6 GCMs that have precipitation represented as independent of vertical mass flux in their deep convection parameterization schemes all simulate decreasing ϵ with warming. This opposes predictions by CRM simulations of projected twenty-first century tropical surface temperatures. GCMs that predict positive $\partial\epsilon/\partial T_s$ show robust additional weakening of the Hadley and Walker circulations, amplified atmospheric warming, and higher sensitivity of extreme precipitation events. Consequently, constraining the sensitivity of ϵ to temperature is critical for quantifying the climate response to anthropogenic forcing.

ACKNOWLEDGEMENTS

The authors thank Dr. Nicholas Lutsko (Scripps Institution of Oceanography) for providing code to compute condensation rates in the cloud-resolving model. We thank Dr. Shineng Hu (Duke University) and Dr. Allison A. Wing (Florida State University) for helpful ideas and discussions. We thank NASA, ECMWF and the CMIP6 group of the World Climate Research Programme for providing free and publicly available data. RL was supported by the National Science Foundation Grant 1352417 and the Yale University Graduate Fellowship. JS and AF acknowledge support from NOAA (NA20OAR4310377). Additional support to AF is provided by the ARCHANGE project (ANR-18-MPGA-0001, the Government of the French Republic). TS was supported by EU H2020 grants 758005 and 821205.

AUTHOR CONTRIBUTIONS STATEMENT

RL and JS conceived the study, performed data analysis, data visualization. RL wrote the original draft and all authors contributed to reviewing and editing the manuscript.

COMPETING INTERESTS STATEMENT

The authors declare no competing interests.

FIGURE CAPTIONS

Fig. 1. Climatology and correspondence of precipitation efficiency index ϵ with temperature. (a) Spatial distributions of annual-mean ϵ in units $10^{-3}s^{-1}$ estimated from satellite observations. Green contours outline regions with 6 mm per day or more surface precipitation in the annual mean. (b) Annual-mean ϵ scattered against surface temperature T_s within the broad Indo-Pacific warm pool region (defined as the left box in panel a). Satellite observations are derived from MODIS and TRMM (see Methods) spanning July 2002 to September 2019.

Fig. 2. Time evolution of $\boldsymbol{\epsilon}$. Observed ϵ and T_s averaged over the entire tropics (30°S–30°N; solid red and blue lines), the Indo-Pacific warm pool (20°S–20°N, 80°E–170°E; dashed lines), and the Eastern Pacific (20°S–20°N, 140°W–80°W; dotted lines). 12-month smoothing is applied to remove the annual cycle. Note several El Niño events, including in 2006, 2009 and 2015.

Fig. 3. Precipitation efficiency ϵ and the large-scale tropical circulation. (a) Temporal correlation coefficients between outgoing longwave radiation (OLR) and annual-mean ϵ_{WP} in satellite observations, with hatching where the p-value for the correlation is lower than 0.05. (b) The strength of the Pacific Walker circulation versus ϵ_{WP} in 44 CMIP6 models, a reanalysis (ERA5), and satellite observations. The line represents a linear regression over all blue points. ϵ_{WP} denotes the spatial average of ϵ over the Indo-Pacific Warm Pool (Box in panel a). Here, east-west sea level pressure difference along the equator, $dSLP$, is used as a measure of the Walker circulation (Methods).

Fig. 4. Sensitivity of ϵ to surface temperature. Changes in precipitation efficiency index ϵ with surface temperature T_s in observations (black squares), ERA5 reanalysis (grey squares), CRMs (diamonds), and 30 CMIP6 GCMs with 22 mass-flux dependent models (Group 1; solid color lines) and 8 mass-flux independent models (Group 2; dashed color lines) in their parameterizations of deep convective precipitation (See Methods). Multi-model mean slopes are estimated by regressing ϵ onto T_s, then taking the average, for Group 1 (solid black line), Group 2 (dashed black line), and all models (dotted black line). Both ϵ and T_s are annual-means and averaged spatially over the entire Tropics (30ºS–30ºN), with the exception of SAM-S (blue diamonds) and SAM-L (red diamonds), which are 15-day and computational domain averages. 10-year smoothing is applied to improve clarity.

Fig. 5. Impact of ϵ on Changes in Temperature and Atmospheric Meridional Circulation under Greenhouse Warming. Difference in the anthropogenic response (defined here as the 2085-2100 average minus the 2015-2030 average in the SSP5-8.5 warming scenario) of (a) zonal-mean temperature (ΔT) and (b) mass streamfunction ($\Delta\psi$; colors) between two groups of CMIP6 GCMs: models with positive $\partial\epsilon/\partial T_s$ (22 models) minus those with negative $\partial\epsilon/\partial T_s$ (8 models) as displayed in Fig. 4. The multi-model-mean zonal-mean circulation averaged from 2015 to 2030 is shown in solid (positive and counter-clockwise) and dotted (negative and clockwise) contours. Hatching represents p-values less than 0.1 using Student's t-test. Note the greater atmospheric warming and more pronounced weakening of the northern Hadley cell for the models with positive $\partial\epsilon/\partial T_s$.

Fig. 6. Role of ϵ in Climate Change. The response to greenhouse warming of the northern (ψ_{max}^N) and southern branches (ψ_{max}^S) of the Hadley circulation, the Pacific Walker circulation (ω_{EP}), and extreme precipitation (global 99.9th percentile daily precipitation, $P_{99.9}$) averaged among two groups of CMIP6 models with positive $\partial\epsilon/\partial T_s$ (red) and negative $\partial\epsilon/\partial T_s$ (blue) under the SSP585 scenario. Maximum zonal-mean streamfunction ψ and eastern equatorial Pacific pressure velocity ω are used as measures of the Hadley and Walker circulations, respectively (*Methods*). Changes are defined as years 2085-2100 minus years 2015-2030. Error bars show multi-model spread. Differences in ψ_{max}^N, ω_{EP} and $P_{99.9}$ have p-values less than 0.05 using Student's t-test. Models with increasing ϵ under greenhouse warming show greater large-scale atmospheric circulation slowdown and a greater increase in extreme rainfall than models with decreasing ϵ.

REFERENCES

[1] Emanuel, Kerry. " Inferences from Simple Models of Slow, Convectively Coupled Processes", *Journal of the Atmospheric Sciences* 76, 1 (2019): 195-208, accessed Feb 23, 2021, https://doi.org/10.1175/JAS-D-18-0090.1

[2] Fowler, H. J., G. Lenderink, A. F. Prein, S. Westra, R. P. Allan, and co-authors, 2021: Anthropogenic intensification of short-duration rainfall extremes. *Nature Reviews Earth and Environment.* https://www.nature.com/articles/s43017-020-00128-6

[3] Narsey, S., C. Jakob, M. S. Singh, and co-authors, 2019: Convective precipitation efficiency observed in the tropics. *GRL.* **46**, 13574-13583. https://agupubs.onlinelibrary.wiley.com/doi/epdf/10.1029/2019GL085031

[4] Singh, M. S., and P. A. O'Gorman, 2014: Influence of microphysics on the scaling of precipitation extremes with temperature, *GRL.* **41** (16), 6037-6044. https://agupubs.onlinelibrary.wiley.com/doi/full/10.1002/2014GL061222.

[5] Lutsko, N. J., and T. W. Cronin, 2018: Increase in precipitation efficiency with surface warming in radiative-convective equilibrium. *JAMES.* **10**, 2992-3010. https://agupubs.onlinelibrary.wiley.com/doi/epdf/10.1029/2018MS001482

[6] Ramanathan, V., , P. J. Crutzen, , J. T. Kiehl, , and D. Rosenfeld, 2001: Aerosols, climate, and the hydrological cycle. *Science*, **294 ,** 2119–2124.

[7] Storer, R. L., & van den Heever, S. C. (2013). Microphysical Processes Evident in Aerosol Forcing of Tropical Deep Convective Clouds, Journal of the Atmospheric Sciences, 70(2), 430-446.

[8] Bao, J., & Sherwood, S. C. (2019). The role of convective self-aggregation in extreme instantaneous versus daily precipitation. *Journal of Advances in Modeling Earth Systems*, 11, 19– 33. https://doi.org/10.1002/2018MS001503

[9] O'Gorman, P. A., 2015: Precipitation Extremes Under Climate Change. *Current Climate Change Reports*. **1**, 49-59. https://link.springer.com/article/10.1007/s40641-015-0009-3

[10] Zhao, Ming. " An Investigation of the Connections among Convection, Clouds, and Climate Sensitivity in a Global Climate Model". *Journal of Climate* 27.5 (2014): 1845-1862. < https://doi.org/10.1175/JCLI-D-13-00145.1>.

[11] Mauritsen, T., & Stevens, B. (2015). Missing iris effect as a possible cause of muted hydrological change and high climate sensitivity in models. Nature Geoscience, 8(346), 346–351.

[12] Tomassini, L., Voigt, A., & Stevens, B. (2015). On the connection between tropical circulation, convective mixing, and climate sensitivity. *Quarterly Journal of the Royal Meteorological Society*, *9*(141), 1404–1416.

[13] Zhao, Ming, J.-C. Golaz, I. M. Held, V. Ramaswamy, S.-J. Lin, Y. Ming, P. Ginoux, B. Wyman, L. J. Donner, D. Paynter, and H. Guo. " Uncertainty in Model Climate Sensitivity Traced to Representations of Cumulus Precipitation Microphysics", *Journal of Climate* 29, 2 (2016): 543-560, accessed Feb 23, 2021, https://doi.org/10.1175/JCLI-D-15-0191.1

[14] Li, R. L., T. Storelvmo, A. V. Fedorov, and Y.-S. Choi. " A Positive Iris Feedback: Insights from Climate Simulations with Temperature-Sensitive Cloud–Rain Conversion". *Journal of Climate* 32.16 (2019): 5305-5324. < https://doi.org/10.1175/JCLI-D-18-0845.1>.

[15] Cohen, C., and E. W. McCaul, 2007: Further Results on the Sensitivity of Simulated Storm Precipitation Efficiency to Environmental Temperature. *Mon. Wea. Rev.*, **135**, 1671–1684, https://doi.org/10.1175/MWR3380.1.

[16] Muller, Caroline J., Paul A. O'Gorman, and Larissa E. Back. " Intensification of Precipitation Extremes with Warming in a Cloud-Resolving Model", *Journal of Climate* 24, 11 (2011): 2784-2800, accessed Feb 23, 2021, https://doi.org/10.1175/2011JCLI3876.1

[17] Lau, K. M., and Wu, H. T. (2003), Warm rain processes over tropical oceans and climate implications, *Geophys. Res. Lett.*, 30, 2290, doi:10.1029/2003GL018567, 24.

[18] Romps, David M. " An Analytical Model for Tropical Relative Humidity". *Journal of Climate* 27.19 (2014): 7432-7449. < https://doi.org/10.1175/JCLI-D-14-00255.1>. Web. 23 Mar. 2021.

[19] Pendergrass, Angeline G., and Dennis L. Hartmann. " The Atmospheric Energy Constraint on Global-Mean Precipitation Change", *Journal of Climate* 27, 2 (2014): 757-768, accessed Mar 6, 2021, https://doi.org/10.1175/JCLI-D-13-00163.1

[20] Flaschner, Dagmar, Thorsten Mauritsen, and Bjorn Stevens. " Understanding the Intermodel Spread in Global-Mean Hydrological Sensitivity", *Journal of Climate* 29, 2 (2016): 801-817, accessed Mar 6, 2021, https://doi.org/10.1175/JCLI-D-15-0351.1

[21] Bony, Sandrine, Bjorn Stevens, David Coppin, Tobias Becker, Kevin A. Reed, Aiko Voigt, Brian Medeiros. "Thermodynamic control of anvil cloud amount", Proceedings of the National Academy of Sciences, 2016, 113 (32) 8927-8932; DOI: 10.1073/pnas.1601472113.

[22] Sui, C.-H., Satoh, M., & Suzuki, K. (2020). Precipitation Efficiency and its Role in Cloud-Radiative Feedbacks to Climate Variability. Journal of the Meteorological Society of Japan. Ser. II, 98(2), 261–282.

[23] Sui, C. H., Li, X., Yang, M. J., & Huang, H. L. (2007). On the definition of precipitation efficiency. Journal of the Atmospheric Sciences, 64(23), 4506–4513.

[24] Market, P., S. Allen, R. Scofield, R. Kuligowski, and A. Gruber, 2003: Precipitation Efficiency of Warm-Season Midwestern Mesoscale Convective Systems. *Wea. Forecasting*, **18**, 1273–1285, https://doi.org/10.1175/1520-0434(2003)018<1273:PEOWMM>2.0.CO;2.

[25] Fankhauser, J. C. " Estimates of Thunderstorm Precipitation Efficiency from Field Measurements in CCOPE". *Monthly Weather Review* 116.3 (1988): 663-684. < https://doi.org/10.1175/1520-0493(1988)116<0663:EOTPEF>2.0.CO;2>.

[26] Ferrier, B. S., , Simpson J. , , and Tao W. K. , 1996: Factors responsible for precipitation efficiencies in midlatitude and tropical squall simulations. *Mon. Wea. Rev.*, **124 ,** 2100–2125.

[27] Pauluis, Olivier, and Isaac M. Held. " Entropy Budget of an Atmosphere in Radiative–Convective Equilibrium. Part I: Maximum Work and Frictional Dissipation", *Journal of the Atmospheric Sciences* 59, 2 (2002): 125-139, accessed Feb 23, 2021, https://doi.org/10.1175/1520-0469(2002)059<0125:EBOAAI>2.0.CO;2

[28] Langhans, Wolfgang, Kyongmin Yeo, and David M. Romps. " Lagrangian Investigation of the Precipitation Efficiency of Convective Clouds", *Journal of the Atmospheric Sciences* 72, 3 (2015): 1045-1062, accessed Feb 23, 2021, https://doi.org/10.1175/JAS-D-14-0159.1

[29] Chong, M., and D. Hauser, 1989: A Tropical Squall Line Observed during the COPT 81 Experiment in West Africa. Part II: Water Budget. *Mon. Wea. Rev.*, **117**, 728–744, https://doi.org/10.1175/1520-0493(1989)117<0728:ATSLOD>2.0.CO;2.

[30] Hobbs, P. V., T. J. Matejka, P. H. Herzegh, J. D. Locatelli, and R. A. Houze, 1980: The Mesoscale and Microscale Structure and Organization of Clouds and Precipitation in Midlatitude Cyclones. I: A Case Study of a Cold Front. *J. Atmos. Sci.*, **37**, 568–596, https://doi.org/10.1175/1520-0469(1980)037<0568:TMAMSA>2.0.CO;2.

[31] Trenberth, K.E. Atmospheric Moisture Residence Times and Cycling: Implications for Rainfall Rates and Climate Change. *Climatic Change* **39,** 667–694 (1998). https://doi.org/10.1023/A:1005319109110

[32] Smalley, K. M. and Rapp, A. D.: A-Train estimates of the sensitivity of the cloud-to-rainwater ratio to cloud size, relative humidity, and aerosols, Atmos. Chem. Phys., 21, 2765–2779, https://doi.org/10.5194/acp-21-2765-2021, 2021.

[33] Pruppacher, H.R., Jaenicke, R., 1995. The processing of water vapor and aerosols by atmospheric clouds, a global estimate. Atmospheric Research 38, 283-295.

[34] Medhaug, I., Stolpe, M., Fischer, E. *et al.* Reconciling controversies about the 'global warming hiatus'. *Nature* **545,** 41–47 (2017). https://doi.org/10.1038/nature22315

[35] Byrne, M.P., Pendergrass, A.G., Rapp, A.D. *et al.* Response of the Intertropical Convergence Zone to Climate Change: Location, Width, and Strength. *Curr Clim Change Rep* **4,** 355–370 (2018). https://doi.org/10.1007/s40641-018-0110-5

[36] Tan, J., C. Jakob, W.B. Rossow, and G. Tselioudis, 2015: Increases in tropical rainfall driven by changes in frequency of organized deep convection. *Nature*, **519**, 451-454, doi:10.1038/nature14339.

[37] Wing, A. A., Stauffer, C. L., Becker, T., Reed, K. A., Ahn, M.-S., Arnold, N. P., . . . Zhao, M. (2020). Clouds and Convective Self-Aggregation in a Multimodel Ensemble of Radiative-Convective Equilibrium Simulations. Journal of Advances in Modeling Earth Systems, 12(9), e2020MS002138.

[38] Emanuel, K., Wing, A. A., and Vincent, E. M. (2014), Radiative-convective instability, *J. Adv. Model. Earth Syst.*, 6, 75– 90, doi:10.1002/2013MS000270.

[39] Wing, A.A., Emanuel, K., Holloway, C.E. *et al.* Convective Self-Aggregation in Numerical Simulations: A Review. *Surv Geophys* **38,** 1173–1197 (2017). https://doi.org/10.1007/s10712-017-9408-4

[40] G.J. Zhang & Norman A. McFarlane (1995) Sensitivity of climate simulations to the parameterization of cumulus convection in the Canadian climate centre general circulation model, Atmosphere-Ocean, 33:3, 407-446, DOI: 10.1080/07055900.1995.9649539

[41] Tiedtke, M. " A Comprehensive Mass Flux Scheme for Cumulus Parameterization in Large-Scale Models". *Monthly Weather Review* 117.8 (1989): 1779-1800. < https://doi.org/10.1175/1520-0493(1989)117<1779:ACMFSF>2.0.CO;2>.

[42] Knutson, Thomas R., and Syukuro Manabe. " Time-Mean Response over the Tropical Pacific to Increased C02 in a Coupled Ocean-Atmosphere Model", *Journal of Climate* 8, 9 (1995): 2181-2199, accessed Feb 23, 2021, https://doi.org/10.1175/1520-0442(1995)008<2181:TMROTT>2.0.CO;2

[43] Held, I. M., and B. J. Soden, 2006: Robust responses of the hydrological cycle to global warming. *J. Climate,* **19,** 5686–5699.

[44] Vallis, G. K., Zurita-Gotor, P., Cairns, C. and Kidston, 2015: Response of the large-scalestructure of the atmosphere to global warming. Q. J. R. Meterol. Soc. 141, 1479-1501.https://rmets.onlinelibrary.wiley.com/doi/epdf/10.1002/qj.2456

[45] Chemke, R., and Polvani, L. M., 2020: Elucidating the mechanisms responsible for Hadley cell weakening under 4xCO_2 forcing. GRL. 48, e2020GL090348. https://agupubs.onlinelibrary.wiley.com/doi/epdf/10.1029/2020GL09048

[46] O'Gorman, P. Sensitivity of tropical precipitation extremes to climate change. *Nature Geosci* **5,** 697–700 (2012). https://doi.org/10.1038/ngeo1568

[47] Myhre, G., Alterskjær, K., Stjern, C.W. *et al.* Frequency of extreme precipitation increases extensively with event rareness under global warming. *Sci Rep* **9,** 16063 (2019). https://doi.org/10.1038/s41598-019-52277-4

[48] Myhre, G., Forster, P. M., Samset, B. H., Hodnebrog, Ø., Sillmann, J., Aalbergsjø, S. G., Andrews, T., Boucher, O., Faluvegi, G., Fläschner, D., Iversen, T., Kasoar, M., Kharin, V., Kirkevåg, A., Lamarque, J.-F., Olivié, D., Richardson, T. B., Shindell, D., Shine, K. P., Stjern, C. W., Takemura, T., Voulgarakis, A., & Zwiers, F. (2017). PDRMIP: A Precipitation Driver and Response Model Intercomparison Project—Protocol and Preliminary Results, Bulletin of the American Meteorological Society, 98(6), 1185-1198.

METHODS

ϵ and the e-folding timescale of condensed water removal

In a static atmosphere, assuming no sources and allowing complete dry out, condensate removal can conceptually be represented by the power law relationship

$$\frac{d}{dt}(CWP) = \alpha(CWP)^{\zeta}, \qquad (2)$$

for a power ζ and inverse timescale α. α in this idealized atmosphere is analogous to ϵ in the real atmosphere. If $\zeta = 1$, Equation (2) becomes the exponential decay equation where CWP has an e-folding timescale of α^{-1}. For $\zeta \neq 1$, the solution is

$$CWP(t) = [\alpha(\zeta - 1)t + 1]^{\frac{1}{1-\zeta}} \; (3)$$

This leads to an e-folding timescale t_e of

$$t_e = \frac{1}{\alpha}\frac{e^{\zeta-1} - 1}{\zeta - 1} = \eta/\alpha,$$

Where η is the correction coefficient for the e-folding timescale of α^{-1}. As η approaches 1, the e-folding timescale approaches α^{-1}. From the satellite observations, $\zeta = 0.64$ and η is 0.84 (Fig. S1). The assumption in Equation (2) of zero condensation sources makes the ϵ^{-1} "drying" timescale an upper bound. In reality, condensing clouds oppose this drying and depart from the e-folding timescale ϵ^{-1}.

Observations

We use monthly liquid water path and ice water path data from the MODerate-resolution Imaging Spectroradiometer (MODIS) Level 3 Atmosphere Monthly Product [49] at 1° by 1° horizontal resolution. For surface precipitation data we use the Tropical Rainfall Measuring Mission (TRMM)

Multisatellite Precipitation Analysis 3B42RT daily precipitation product [50]. Its native horizontal resolution of 0.25° by 0.25° was re-gridded to 1° by 1° to match the MODIS data. Measurements of monthly top-of-atmosphere longwave radiative fluxes used in this study were from the Clouds and Earth's Radiation Energy System (CERES) SYN1deg-Ed4A product, which combines data from Aqua and Terra [51]. Monthly gridded surface temperature data (land and ocean) are from the Berkeley Earth Surface Temperatures dataset, available at http://berkeleyearth.org/archive/data/. Monthly SLP data is from the Hadley Centre Sea Level Pressure Dataset [52], available at https://psl.noaa.gov/data/gridded/data.hadslp2.html.

Uncertainty in Precipitation and Cloud Water Path Observations

Observed liquid water path (LWP) and ice water path (IWP) are in-cloud values. These are weighted by cloud fraction to render them comparable with the models' grid-box averaged cloud water path, computed by the following expression at each grid point:

$$CWP_{obs} = f_{obs}(IWP_{obs} + LWP_{obs})$$

Where the subscript *obs* indicates observational data and f is cloud fraction.

Uncertainty in ϵ can be estimated using the individual uncertainties in P_s and CWP. MODIS sensors are calibrated with high accuracy. Ref [53] conducted an analysis of available satellite estimates of LWP against passive microwave observations and found that MODIS outperforms all other satellite observational products. In the three regions they analyzed, MODIS estimates generally underestimate the monthly-mean LWP by 8-9% relative to terrestrial microwave estimates. However, the correlation coefficient between monthly MODIS and microwave data is 0.9. Similar estimates are unavailable for IWP. TRMM exhibits lower errors than other real-time precipitation observational products at most temporal scales. Ref [54] analyzed monthly surface precipitation (P_s) data over the maritime continents and found that TRMM underestimates P_s by 6% compared to rain gauge measurements, with a monthly correlation coefficient of $r = 0.86$. Using the error estimates, 6% in P_s and 9% in CWP (assuming that IWP uncertainties are similar magnitude to the LWP range), we estimate the uncertainty of ϵ

$$\frac{\Delta\epsilon}{\epsilon} = \left[\left(\frac{\Delta P_s}{P_s}\right)^2 + \left(\frac{\Delta CWP}{CWP}\right)^2\right]^{\frac{1}{2}} \approx 11\%$$

ERA5 Reanalysis

Data from the ERA5 Reanalysis [55] are obtained from the Climate Data Store (available at https://cds.climate.copernicus.eu/cdsapp#!/dataset/reanalysis-era5-pressure-levels-monthly-means) and interpolated to the same grid as the observations (1° by 1° resolution).

CRM experiments

Idealized experiments of radiative convective equilibrium in limited domains are performed using the System for Atmospheric Modeling (SAM; [56]), three-dimensional cloud resolving model that employs the anelastic equations of motion. As in previous studies of convective self-aggregation with SAM, we use a 1-moment microphysics package. The model grid is a staggered Arakawa C-type grid with a uniform horizontal resolution of 2 km and stretched in the vertical. The lowest model level is 37 m and the grid spacing is 75 m, increasing to 500 m above 3.5 km. The lateral boundary conditions are doubly periodic. We achieve radiative-convective equilibrium by forcing the model with perpetual sun (no diurnal cycle), no mean wind, no rotation, and no other external forcing. Independent experiments were run with fixed SSTs at 299K, 300K, 301K, and 303K. The two sets of experiments shown in Fig. 4 are SAM-S and SAM-L which employ a 512 x 512 km^2 domain and a 1024 x 1024 km^2 domain, respectively.

All SAM-L experiments self-aggregate to form a single cluster of convection after day 80 of the simulation. The SAM-S experiments do not self-aggregate due to the domain size limitation. This domain size dependence of self-aggregation has been previously well studied [57, 58]. We used the domain-size difference between SAM-L and SAM-S to isolate the effects of self-aggregation while keeping the external forcing identical. Each experiment is averaged from day 80 to 100 after reaching statistical equilibrium.

CMIP6 Models

We use the CMIP6 archive [59] to obtain data for 44 GCMs in the preindustrial control simulation (piControl) and 28 models in the SSP585 scenario. This represents all models with available output to compute ϵ at the time of analysis. Warming responses are computed by taking the difference between years 2085-2100 and years 2015-2030 in the SSP585 scenario.

Parameterization of Convective Precipitation in CMIP6 Models

The two representative convective parameterization schemes in CMIP6 are the Tiedtke scheme ([42]; hereafter T89) and the Zhang and McFarlane scheme ([41]; hereafter ZM95). In T89, deep convection is triggered when there is net water vapor convergence in the atmospheric column and air lifted from the surface to above cloud base remains buoyant. The conversion from cloud droplets to convective precipitation is given by:

$$P_{T89}(z) = K(z)l$$

where $P_{T89}(z)$ is the precipitation rate at height z, l is the cloud water content in mm, and K(z) is a step function that takes the value of $0.002s^{-1}$ above a constant offset above cloud base and zero elsewhere. P_{T89} depends only on the cloud water content.

In ZM95, deep convection is triggered in a column if the convective available potential energy, after accounting for dilution from entrainment of dry air, exceeds $70\,Jkg^{-1}$. Convective precipitation is given by the following expression [60]:

$$\rho P_{ZM95}(z) = C_0 M_u l$$

where $C_0 = 0.002m^{-1}$, M_u is the updraft mass flux, and ρ is the air density, and l is the cloud water content. P_{ZM95} is proportional to both M_u and l.

Strength of the Pacific Walker Circulation

Following [61], to measure the mean strength of the Pacific Walker circulation (Fig. 3b) we compute Sea Level Pressure (*SLP*) averaged over the equatorial Western Pacific (SLP_W; 5°S–5°N, 80°–160°E) and equatorial Eastern Pacific (SLP_E; 5°S–5°N, 160°–80°W), and use their difference, denoted as $dSLP$:

$$dSLP = SLP_E - SLP_W$$

To measure projected changes in the strength of the Walker circulation, we compute the average pressure velocity at $800hPa$ over the equatorial Eastern Pacific (ω_{EP}; 10°S–10°N, 160°E–100°W). This definition shows the strongest correlation with changes in the SST gradient between the eastern and western equatorial Pacific, in which the Pacific Walker Circulation is tightly coupled to. We find that this measure provides more robust results on future Walker cell changes across different models as it is less dependent on the choice of the averaging boxes than *dSLP*.

Strength of the Hadley Circulation

To measure the strength of the Hadley circulation, we firstly estimate the ITCZ location (ϕ_{ITCZ}) defined as the zeroth crossing of the zonal-mean mass streamfunction ψ closest to the equator. The Hadley cell's meridional extent in each hemisphere is the distance between ϕ_{ITCZ} and the first zeroth crossing of ψ poleward of ϕ_{ITCZ}. The strength of the Hadley Circulation in each hemisphere is estimated by taking the maximum of ψ between 700 and 300 hPa throughout its meridional extent [62].

DATA AVAILABILITY

TRMM data is obtained from https://gpm.nasa.gov/missions/trmm are interpolated from their native 0.25° by 0.25° resolution to 1° by 1° to match that of the MODIS monthly data available at https://atmosphere-imager.gsfc.nasa.gov/products/monthly. Monthly surface temperature (http://berkeleyearth.org/archive/data/) and SLP observations (https://psl.noaa.gov/data/gridded/data.hadslp2.html) are also publicly available. Monthly-mean Nino 3.4 SST data is obtained from: https://www.ncdc.noaa.gov/teleconnections/enso/indicators/sst/. ERA5 data are downloaded from https://cds.climate.copernicus.eu/cdsapp#!/dataset/reanalysis-era5-pressure-levels-monthly-means and interpolated from their native 0.25° by 0.25° grid to 1° by 1° resolution. The CMIP6 data supporting this study are available from https://pcmdi.llnl.gov/CMIP6/. Data from the CRM experiments and satellite derived observations of ϵ are available at https://doi.org/10.5061/dryad.g4f4qrfsr [63].

METHODS-ONLY REFERENCES

[49] Platnick, S., M. King, P. Hubanks, 2017. MODIS Atmosphere L3 Monthly Product. NASA MODIS Adaptive Processing System, Goddard Space Flight Center, [doi:10.5067/MODIS/MOD08_M3.061; doi:10.5067/MODIS/MYD08_M3.061]

[50] Huffman, George J., David T. Bolvin, Eric J. Nelkin, David B. Wolff, Robert F. Adler, Guojun Gu, Yang Hong, Kenneth P. Bowman, and Erich F. Stocker. " The TRMM Multisatellite Precipitation Analysis (TMPA): Quasi-Global, Multiyear, Combined-Sensor Precipitation Estimates at Fine Scales". *Journal of Hydrometeorology* 8.1 (2007): 38-55. < https://doi.org/10.1175/JHM560.1>.

[51] Wielicki, Bruce A., Bruce R. Barkstrom, Edwin F. Harrison, Robert B. Lee, III, G. Louis Smith, and John E. Cooper. " Clouds and the Earth's Radiant Energy System (CERES): An Earth Observing System Experiment". *Bulletin of the American Meteorological Society* 77.5 (1996): 853-868. < https://doi.org/10.1175/1520-0477(1996)077<0853:CATERE>2.0.CO;2>.

[52] Allan, R. and T. Ansell, 2006: A New Globally Complete Monthly Historical Gridded Mean Sea Level Pressure Dataset (HadSLP2): 1850–2004. J. Climate, 19, 5816–5842, https://doi.org/10.1175/JCLI3937.1.

[53] Stengel, M., Stapelberg, S., Sus, O., Schlundt, C., Poulsen, C., Thomas, G., Christensen, M., Carbajal Henken, C., Preusker, R., Fischer, J., Devasthale, A., Willén, U., Karlsson, K.-G., McGarragh, G. R., Proud, S., Povey, A. C., Grainger, R. G., Meirink, J. F., Feofilov, A., Bennartz, R., Bojanowski, J. S., and Hollmann, R.: Cloud property data sets retrieved from AVHRR, MODIS, AATSR and MERIS in the framework of the Cloud_CCI project, Earth Syst. Sci. Data, 9, 881-904, https://doi.org/10.5194/essd-9-881-2017, 2017.

[54] Rauniyar, S. P., Protat, A., and Kanamori, H. (2017), Uncertainties in TRMM-Era multisatellite-based tropical rainfall estimates over the Maritime Continent, Earth and Space Science, 4, 275– 302, doi:10.1002/2017EA000279.

[55] Hersbach, H., Bell, B., Berrisford, P., Biavati, G., Horányi, A., Muñoz Sabater, J., Nicolas, J., Peubey, C., Radu, R., Rozum, I., Schepers, D., Simmons, A., Soci, C., Dee, D., Thépaut, J-N. (2019): ERA5 monthly averaged data on pressure levels from 1979 to present. Copernicus Climate Change Service (C3S) Climate Data Store (CDS). https://doi.org/10.24381/cds.6860a573.

[56] Khairoutdinov, Marat F., and David A. Randall. " Cloud Resolving Modeling of the ARM Summer 1997 IOP: Model Formulation, Results, Uncertainties, and Sensitivities". *Journal of the Atmospheric Sciences* 60.4 (2003): 607-625. < https://doi.org/10.1175/1520-0469(2003)060<0607:CRMOTA>2.0.CO;2>.

[57] Muller, C.J. and I.M. Held, 2012: Detailed Investigation of the Self-Aggregation of Convection in Cloud-Resolving Simulations. *J. Atmos. Sci.,* **69**, 2551–2565, https://doi.org/10.1175/JAS-D-11-0257.1

[58] Wing, A. A., and K. A. Emanuel, 2014: Physical mechanisms controlling self-aggregation of convection in idealized numerical modeling simulations. J. Adv. Model. Earth Syst., 6, 59–74, https://doi.org/10.1002/2013MS000269.

[59] Eyring, V., Bony, S., Meehl, G. A., Senior, C. A., Stevens, B., Stouffer, R. J., and Taylor, K. E.: Overview of the Coupled Model Intercomparison Project Phase 6 (CMIP6) experimental design and organization, Geosci. Model Dev., 9, 1937–1958, https://doi.org/10.5194/gmd-9-1937-2016, 2016.

[60] Lord, S.J., W.C. Chao, and A. Arakawa, 1982: Interaction of a Cumulus Cloud Ensemble with the Large-Scale Environment. Part IV: The Discrete Model. *J. Atmos. Sci.,* **39**,104–113, https://doi.org/10.1175/1520-0469(1982)039<0104:IOACCE>2.0.CO;2

[61] Vecchi, G. A., , and B. J. Soden, 2007: Global warming and the weakening of the tropical circulation. *J. Climate*, **20**, 4316–4340, doi:10.1175/JCLI4258.1.

[62] Nguyen, H., A. Evans, C. Lucas, I. Smith, and B. Timbal, 2013: The Hadley circulation in reanalysis: Climatology, variability, and change, *J. Climate.* **26**, 3357-3376. https://journals.ametsoc.org/view/journals/clim/26/10/jcli-d-12-00224.1.xml

[63] Li, Ryan (2022), Precipitation Efficiency Constraint on Climate Change Data, Dryad, Dataset, https://doi.org/10.5061/dryad.g4f4qrfsr.

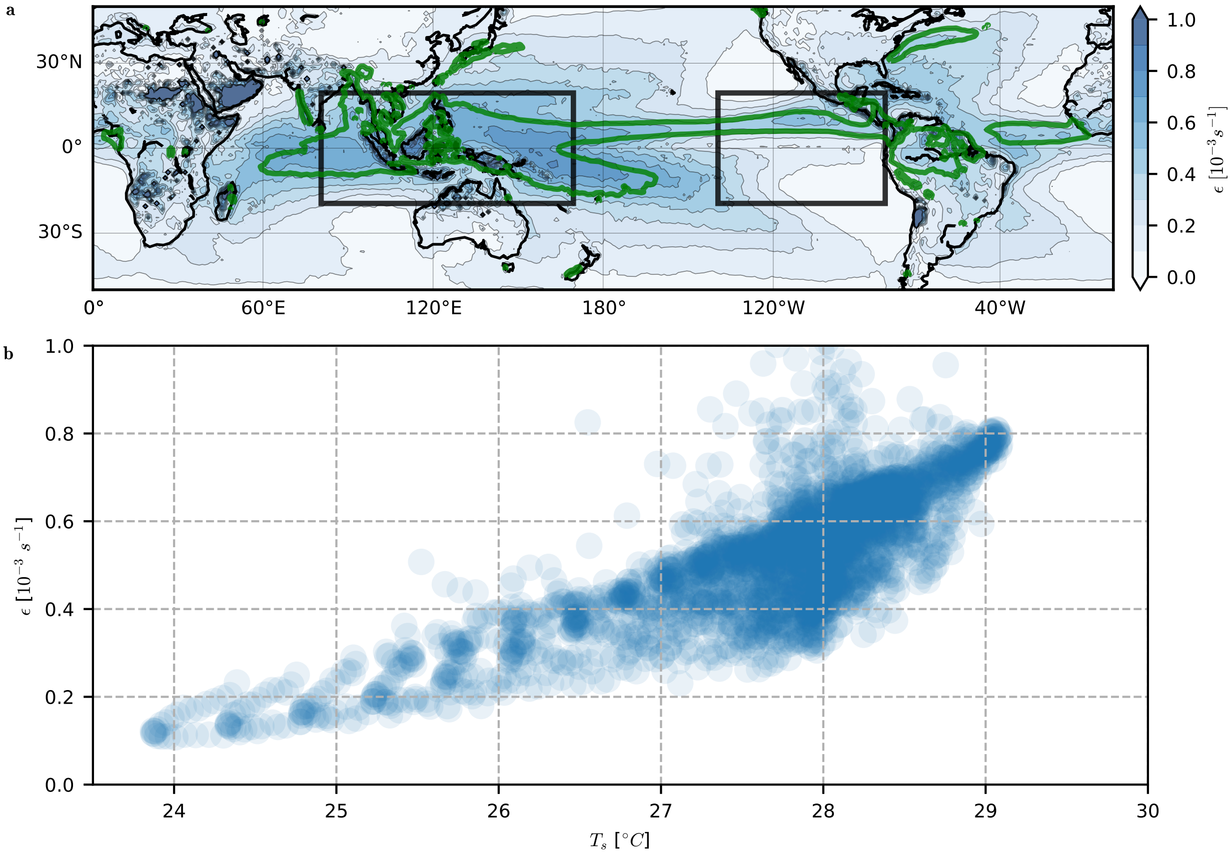
a
30°N
0°
30°S
0°
60°E
120°E
180°
120°W
40°W
1.0
0.8
0.6
0.4
0.2
0.0
ϵ $[10^{-3} s^{-1}]$
b
1.0
0.8
0.6
0.4
0.2
0.0
ϵ $[10^{-3}\ s^{-1}]$
24
25
26
27
28
29
30
T_s $[^\circ C]$

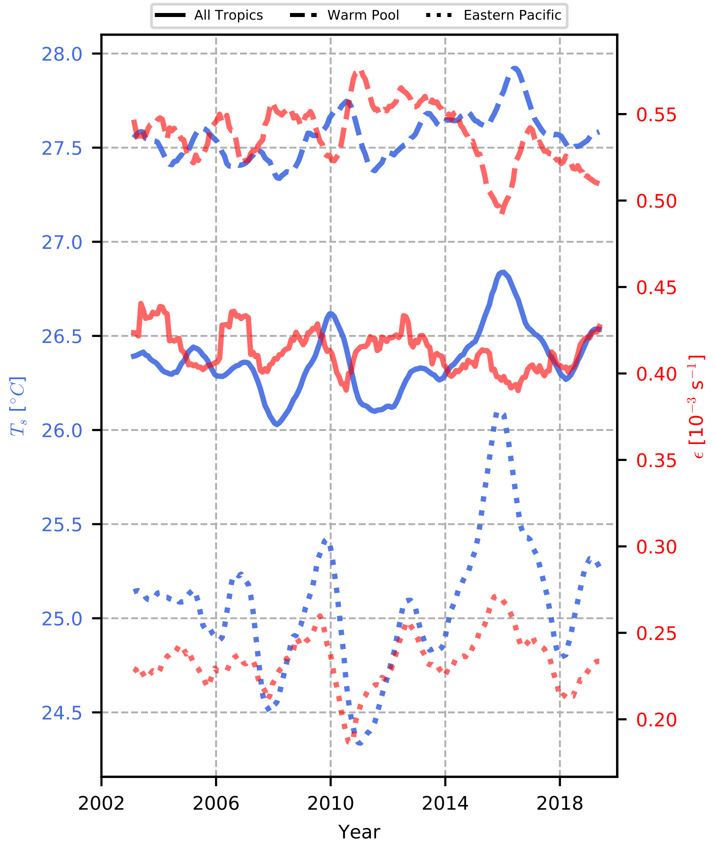

All Tropics
Warm Pool
Eastern Pacific
T_s [$^\circ C$]
28.0
27.5
27.0
26.5
26.0
25.5
25.0
24.5
ϵ [10^{-3} s^{-1}]
0.55
0.50
0.45
0.40
0.35
0.30
0.25
0.20
2002
2006
2010
2014
2018
Year

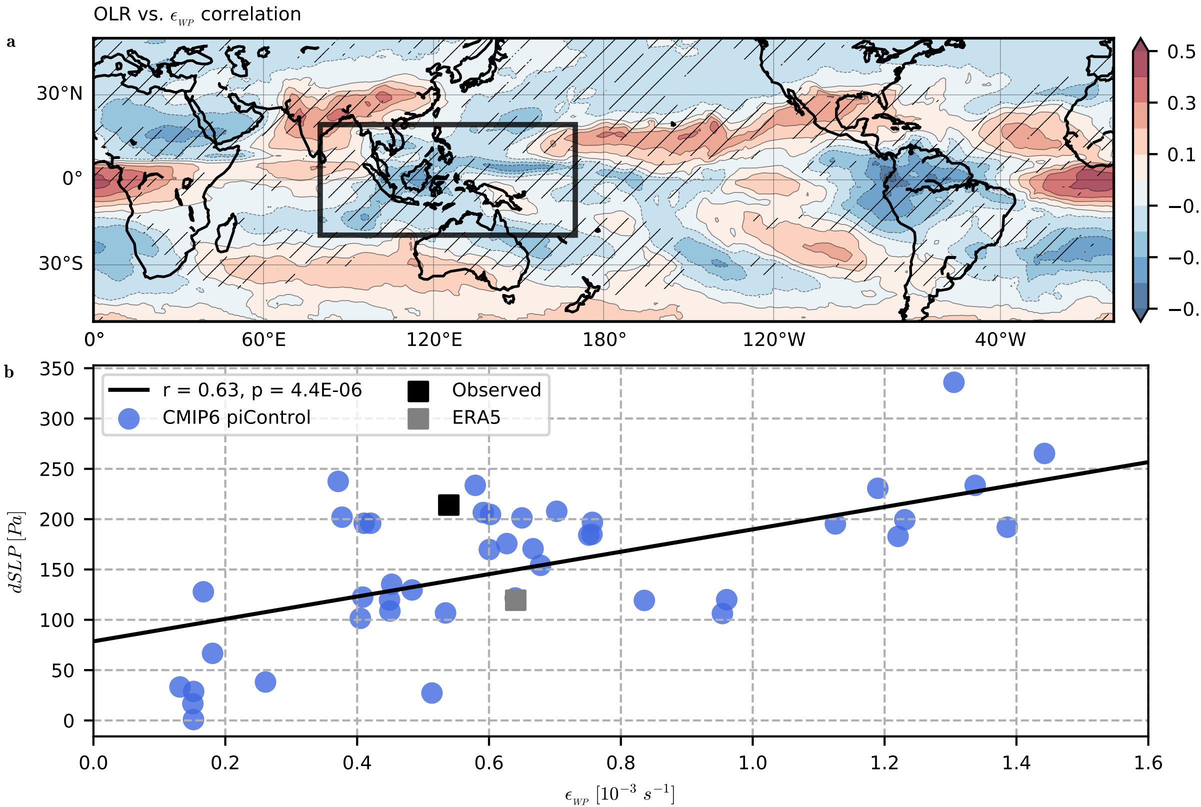

OLR vs. ϵ_{WP} correlation
a
30°N
0°
30°S
0°
60°E
120°E
180°
120°W
40°W
0.5
0.3
0.1
−0.1
−0.3
−0.5
b
r = 0.63, p = 4.4E-06
CMIP6 piControl
Observed
ERA5
$dSLP\ [Pa]$
$\epsilon_{WP}\ [10^{-3}\ s^{-1}]$
0
50
100
150
200
250
300
350
0.0
0.2
0.4
0.6
0.8
1.0
1.2
1.4
1.6

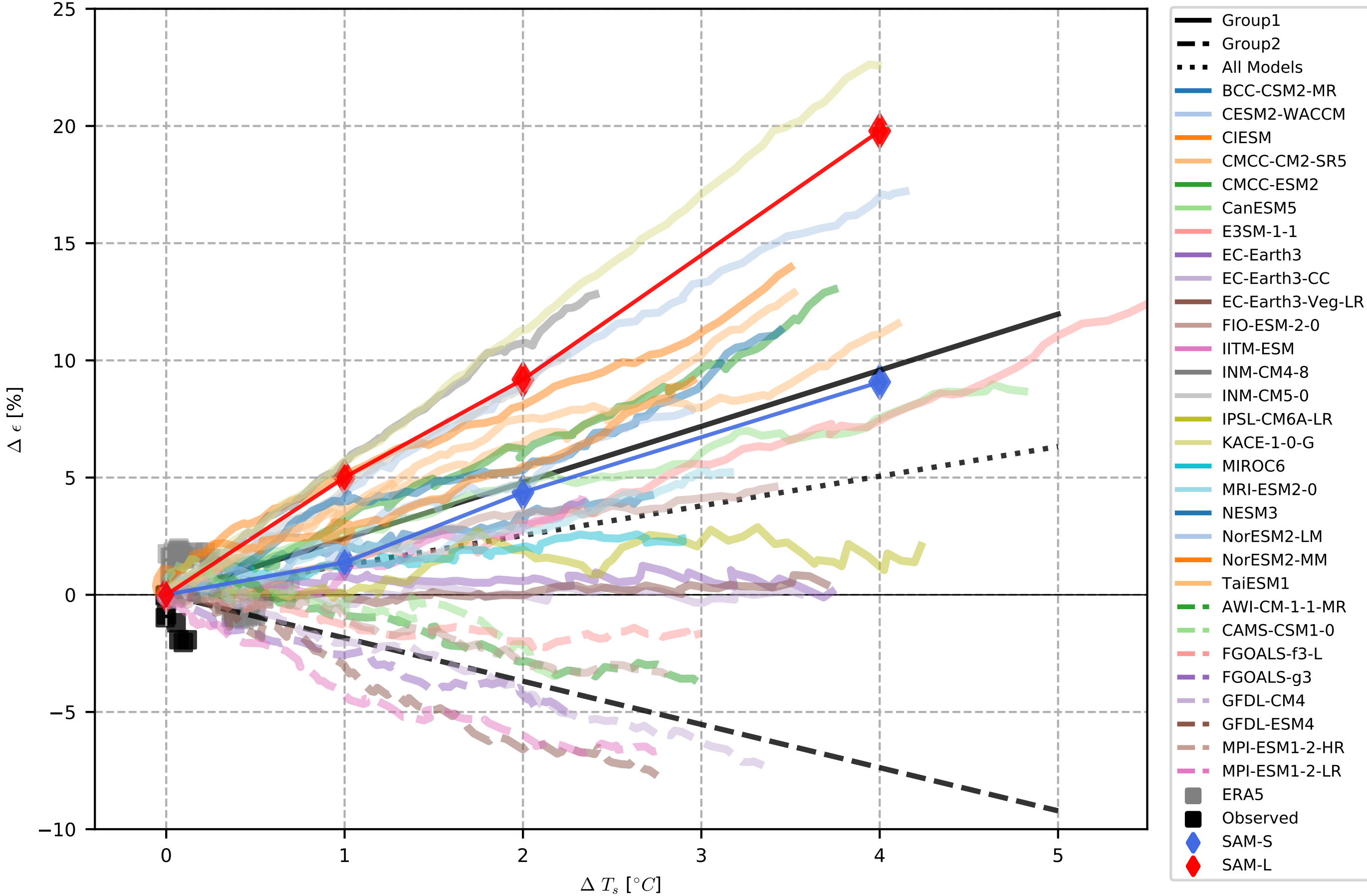

Group1
Group2
All Models
BCC-CSM2-MR
CESM2-WACCM
CIESM
CMCC-CM2-SR5
CMCC-ESM2
CanESM5
E3SM-1-1
EC-Earth3
EC-Earth3-CC
EC-Earth3-Veg-LR
FIO-ESM-2-0
IITM-ESM
INM-CM4-8
INM-CM5-0
IPSL-CM6A-LR
KACE-1-0-G
MIROC6
MRI-ESM2-0
NESM3
NorESM2-LM
NorESM2-MM
TaiESM1
AWI-CM-1-1-MR
CAMS-CSM1-0
FGOALS-f3-L
FGOALS-g3
GFDL-CM4
GFDL-ESM4
MPI-ESM1-2-HR
MPI-ESM1-2-LR
ERA5
Observed
SAM-S
SAM-L
$\Delta\ \epsilon$ [%]
$\Delta\ T_s$ [$^\circ C$]
25
20
15
10
5
0
−5
−10
0
1
2
3
4
5

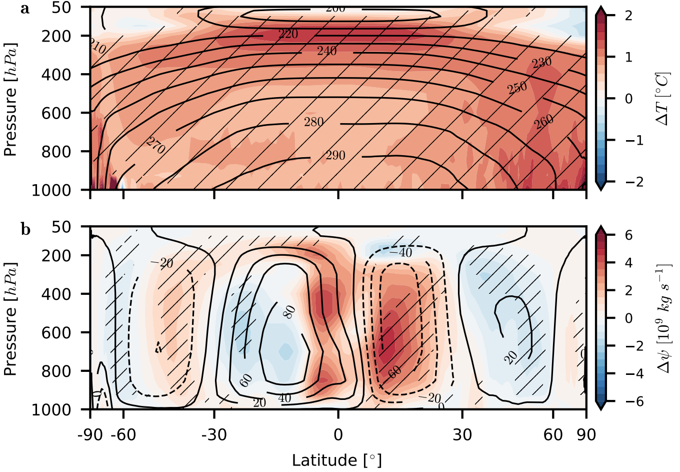

a
b
Pressure [hPa]
Latitude [$^\circ$]
$\Delta T\ [^\circ C]$
$\Delta\psi\ [10^9\ kg\ s^{-1}]$
50
200
400
600
800
1000
-90
-60
-30
0
30
60
90
2
1
0
−1
−2
6
4
2
0
−2
−4
−6
200
210
220
230
240
250
260
270
280
290
−20
−40
20
40
60
80

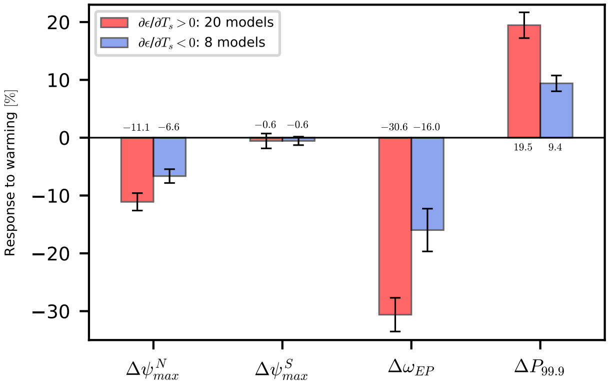

$\partial\epsilon/\partial T_s > 0$: 20 models
$\partial\epsilon/\partial T_s < 0$: 8 models
Response to warming [%]
20
10
0
−10
−20
−30
−11.1
−6.6
−0.6
−0.6
−30.6
−16.0
19.5
9.4
$\Delta\psi^N_{max}$
$\Delta\psi^S_{max}$
$\Delta\omega_{EP}$
$\Delta P_{99.9}$